





Derivation of coherent-population-trapping resonance signals from density-matrix equations with all relevant sublevels of Cs atoms and confirmation of experimental results

Kenta Matsumoto ^{1,2}, Sota Kagami,^{1,2} Takahiro Fujisaku,^{1,2} Akihiro Kirihara,^{1,2} Shinya Yanagimachi ³, Takeshi Ikegami ⁴ and Atsuo Morinaga ⁴

¹Secure System Platform Research Laboratories, NEC Corporation, 1753 Shimonumabe, Nakahara-ku, Kawasaki, Kanagawa 211-0011, Japan

²National Institute of Advanced Industrial Science and Technology, NEC-AIST Quantum Technology Cooperative Research Laboratory, 1-1-1 Umezono, Tsukuba, Ibaraki 305-8568, Japan

³National Institute of Advanced Industrial Science and Technology, 1-1-1 Umezono, Tsukuba, Ibaraki 305-8563, Japan

⁴Micromachine Center, AIST Tsukuba East 4G, 1-2-1 Namiki, Tsukuba, Ibaraki 305-8564, Japan



(Received 8 July 2024; accepted 29 July 2024; published 27 August 2024)

Coherent-population-trapping resonance in vapor cell is a quantum interference effect that appears in the two-photon transitions between the ground-state hyperfine levels of alkali-metal atoms and is often utilized in miniature and centimeter-scale clock devices. To quantitatively understand and predict the performance of this phenomenon, it is necessary to consider the transitions and relaxations between all hyperfine Zeeman sublevels involved in the different excitation processes of the atom. In this paper, we constructed a computational multilevel atomic model of the Liouville density-matrix equation for 32 Zeeman sublevels involved in the D_1 line of ^{133}Cs irradiated by two frequencies with circularly polarized components and then simulated the amplitude and shape of the resonance spectrum of the transmitted light through centimeter-scale Cs-vapor cells. We show that the numerical solutions of the equation and analytical investigations adequately explain a variety of the characteristics observed in the experiment.

DOI: [10.1103/PhysRevA.110.023113](https://doi.org/10.1103/PhysRevA.110.023113)

I. INTRODUCTION

Coherent-population-trapping (CPT) resonance is a quantum interference phenomenon observed using a two-photon Λ -type transition between the ground hyperfine Zeeman sublevels of an alkali-metal atom [1,2]. Thanks to its high Q factor at the microwave transition, it is currently utilized as a key spectroscopic technique for creating portable atomic clock devices [3]. In more than 20 years following the first detection of CPT resonance in vapor cells [4,5] and proposal for microfabricated atom vapor cells [6–8], ongoing advancements have led to the development of miniature atomic clocks using silicon micromachining and semiconductor laser technology [9], the achievement of high contrast signals [10], and increased robustness of the resonance frequency to fluctuations in the external environment and the excitation light itself [11,12].

The optical excitation scheme originally utilized in the CPT clock is a circular polarization for bichromatic excitation lights, $\sigma^- \text{-} \sigma^-$ or $\sigma^+ \text{-} \sigma^+$, but such polarization pumps a significant fraction of the atoms into Zeeman edge (trap) states, thus reducing the contrast of the CPT signal. To prevent this reduction, excitation schemes such as push-pull optical pumping [13], counterpropagating $\sigma^+ \text{-} \sigma^-$ polarization [14], a pair of orthogonal linear polarizations (Lin \perp Lin) [15], or a pair of parallel linear polarizations (Lin \parallel Lin) [16] have been proposed. The first three methods produce the CPT resonance between two hyperfine states $|F_g = 3, m = 0\rangle$ and $|F_e = 4, m = 0\rangle$ on each leg of the Λ scheme, namely (0, 0) CPT resonance [17]. This resonance is

essentially a double- Λ scheme, in which a dark state common to the two Λ schemes exists [18]. In contrast, no (0, 0) CPT resonance occurs in the fourth method because the dark state for one Λ scheme is the bright state for the other. Instead, two CPT resonances are produced between $|F_g, m = -1\rangle$ and $|F_e, m = 1\rangle$ and between $|F_g, m = 1\rangle$ and $|F_e, m = -1\rangle$, namely (−1, 1) and (1, −1) CPT resonances. These doublet resonances split in frequency due to the second-order Zeeman effect [19]. The relationship between the CPT resonance and excitation polarization scheme on ^{133}Cs atoms has been studied by Liu *et al.* [17].

In our previous work [20], we showed that the amplitudes of the (−1, 1) and (1, −1) CPT resonances excited with Lin \parallel Lin polarization increase approximately in proportion to the excitation intensity, while in contrast, the amplitude of the (0, 0) CPT resonance excited with $\sigma^- \text{-} \sigma^-$ polarization moderately saturates. We claimed that the former is best described by a simple three-level model and the latter by a four-level model with a trap state. Up to now, the symmetry, width, and frequency shift of the resonance spectrum related to the optical detuning of the excitation lights were investigated using few-level models [21,22]. However, a model that includes all Zeeman sublevels will be effective for quantitatively understanding the amplitude, the width, and the shape of the CPT resonances [23]. These behaviors of the CPT spectrum can be better understood by solving the Liouville density-matrix equation taking into account 32 Zeeman sublevels related to the D_1 line of ^{133}Cs .

When constructing a model with 32 Zeeman sublevels, it is necessary to configure a detailed relaxation process between

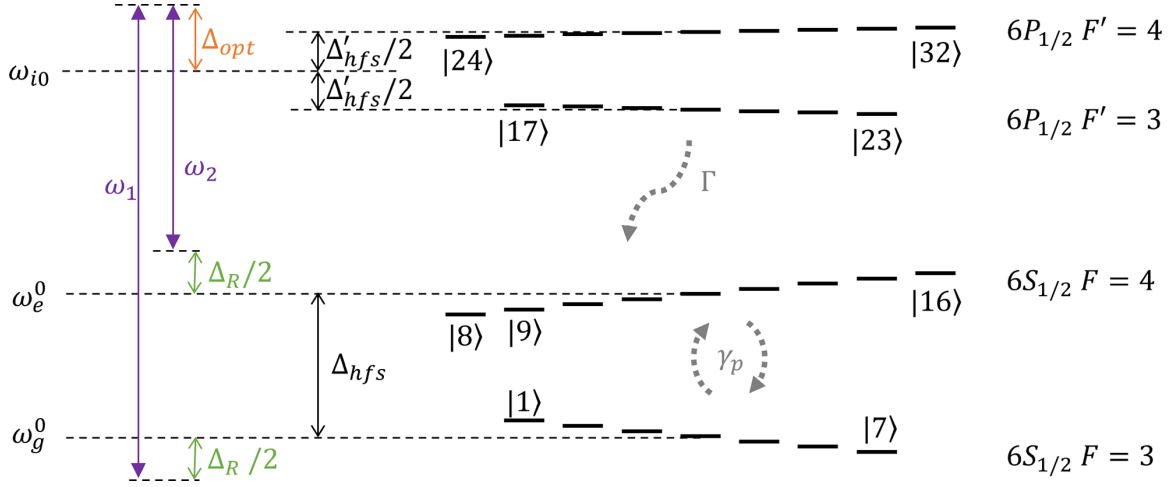


FIG. 1. Hyperfine Zeeman structure of the D_1 line of ^{133}Cs . Values are expressed in the unit of angular frequency. |1) – |7), |8) – |16), |17) – |23), and |24) – |32) are the magnetic sublevels of $6S_{1/2}F = 3$, $6S_{1/2}F = 4$, $6P_{1/2}F' = 3$, and $6P_{1/2}F' = 4$, respectively, labeled in order of magnetic quantum number m_F from $-F$ to F . ω_g^0 and ω_e^0 are unperturbed energies of $6S_{1/2}F = 3$ and 4, respectively. ω_{i0} is the medium energy between the unperturbed energies of $6P_{1/2}F' = 3$ and 4. Δ_{hfs} and Δ'_{hfs} are the hyperfine splitting energies of $6S_{1/2}$ and $6P_{1/2}$, respectively. ω_1 and ω_2 are frequencies of the excitation lights in a unit of angular frequency. Δ_R and Δ_{opt} are the Raman detuning and the common detuning, respectively, which are defined in the paper. Γ and γ_p are the decay rate of $6P_{1/2}$ (excited) states and $6S_{1/2}$ (ground) states, respectively.

16 ground levels, though it is simple in the three-level model because there are only two ground levels. In 2017, Warren *et al.* developed an atomic model using the Liouville density-matrix equation taking into account all 16 relevant Zeeman sublevels in the D_1 line of ^{87}Rb atoms and compared the calculated results with the corresponding experimental results for excitation with three different polarization configurations [24]. They assumed a uniform relaxation process between the magnetic sublevels of the ground states. In an alternative approach, Matsuda *et al.* utilized the magnetic dipole relaxation between the magnetic sublevels of the ground states in the D_1 line of ^{133}Cs atoms [25].

We make two key contributions in the current paper. First, we construct a multilevel atomic model of the Liouville density-matrix equation [23–26] for studying CPT resonances formed by the bichromatic lights of various excitation schemes in the manifold of ^{133}Cs atoms. Second, using the constructed model, we simulate the amplitude and shape of the CPT resonance excited by different polarizations, frequencies, and intensities of the excitation lights, and elucidate the underlying mechanisms by comparing them with the corresponding experimental results. In Sec. II A, we derive the multilevel atomic model using the density-matrix equation, and in Sec. II B, we show the formulations for the line shape, width, and light shift of the CPT resonance spectrum guided from the present multilevel atomic model. Section III describes our experimental setup and Cs-vapor cells with buffer gas. In Sec. IV, we compare the experimental results with the calculated results. Section IV A reports how the Zeeman CPT spectra with different buffer gas pressures vary due to the relaxation process. Section IV B shows that the amplitude of the first-order Zeeman CPT spectra depends on the common detuning frequency of the excitation light. In Sec. IV C, we clarify that the (m, m) CPT resonance appears for Lin \parallel Lin excitation [except for $(0, 0)$] in the second-order

Zeeman CPT spectrum and discuss the required conditions to prohibit the CPT resonances of double- Λ schemes. Section IV D explains how the amplitude of the CPT resonance for $\sigma^- - \sigma^-$ excitation saturates while that for Lin \parallel Lin excitation increases in proportion to the excitation intensity depending on the variation of the population in the trap state. We conclude in Sec. V with a brief summary. The Appendix provides additional detail on how the shape of the CPT spectrum is rigorously derived from the 32-level model.

II. FORMULATION AND CALCULATION

A. Liouville equations for the CPT spectrum

We aim to construct a multilevel atomic model including all the Zeeman sublevels in the D_1 transition of ^{133}Cs so as to theoretically investigate the CPT resonances excited with various polarizations. Figure 1 shows the energy structure of the hyperfine Zeeman sublevels in the D_1 line of ^{133}Cs under a magnetic field as a perturbation together with the definition of the energy detuning of the bichromatic excitation lights for the CPT resonance, whose angular frequencies are ω_1 and ω_2 . In this paper, all quantities of the energy detuning and energy levels are given in the unit of angular frequency. We designate sublevels belonging to $6S_{1/2}F = 3$, $F = 4$, and $6P_{1/2}F' = 3$ or $F' = 4$ as g , e , and i , respectively. The unperturbed energies of the hyperfine ground states, $6S_{1/2}F = 3$ and $F = 4$, are represented as ω_g^0 and ω_e^0 , respectively. ω_{i0} is the mean energy between the unperturbed energies of $6P_{1/2}F' = 3$ and $F' = 4$. We define the propagation direction of the bichromatic lights as along the z axis and the quantized magnetic field with strength B as applied along the direction of the light propagation. We also define energies of the Zeeman sublevels under the magnetic field B as ω_g^B , ω_e^B , and ω_i^B , which are shifted by the Zeeman effect according to Breit-Rabi's formula [19]. Then, there are 32 Zeeman sublevels in the hyperfine ground

states, $6S_{1/2}F = 3$ and $F = 4$, and in the hyperfine excited states, $6P_{1/2}F' = 3$ and $F' = 4$, some of which are coupled by the D_1 transition depending on the polarization of excitation lights. As shown in Fig. 1, Zeeman sublevels are designated from 1 to 32 in order of the magnetic quantum numbers m_F from $-F$ to F , and from g to i .

The two photons ω_1 and $\omega_2 (< \omega_1)$ induce a three-level Λ -type CPT resonance between the two hyperfine levels in the ground state and an excited level. The energy detuning of ω_1 from the related D_1 transition energy is $\Delta_1 = \omega_1 - (\omega_{i0} - \omega_g^0)$. Similarly, that of ω_2 is $\Delta_2 = \omega_2 - (\omega_{i0} - \omega_e^0)$. The Raman detuning of $\omega_1 - \omega_2$ from the ground hyperfine splitting ($\Delta_{\text{hfs}} = \omega_e^0 - \omega_g^0$) is given by $\Delta_R = (\omega_1 - \omega_2) - \Delta_{\text{hfs}}$. In the CPT resonance experiment, generally, the positive first and negative first sidebands generated from a single laser source by modulating at a frequency of $(\Delta_{\text{hfs}} + \Delta_R)/2$ are used as the two photons ω_1 and ω_2 . As shown in Fig. 1, we define the common detuning Δ_{opt} as $\Delta_{\text{opt}} = \Delta_1 - \frac{\Delta_R}{2} = \Delta_2 + \frac{\Delta_R}{2}$.

The system with a set of the orthonormal quantum states $|1\rangle - |32\rangle$ corresponding to the 32 magnetic sublevels of a Cs atom (presented in Fig. 1) is described by the Heisenberg equation of the density-matrix component ρ and the interaction Hamiltonian H , as

$$\frac{\partial}{\partial t} \rho = \frac{1}{i\hbar} [\mathcal{H}, \rho] \quad (1)$$

where \hbar is the Planck constant divided by 2π . The coupling of the atomic states to two coherent radiation fields is described within the rotating wave approximation, as

$$\frac{1}{\hbar} \mathcal{H} = \sum_{l=1}^{32} \delta_l |l\rangle \langle l| - \frac{1}{2} \sum_{s=1}^{16} \sum_{t=17}^{32} (\Omega_{\text{st}} |s\rangle \langle t| + \Omega_{\text{st}}^* |t\rangle \langle s|) \quad (2)$$

where

$$\delta_l = \begin{cases} \omega_l^B - \omega_g^0 + \frac{\Delta_R}{2} & l = 1, \dots, 7 \\ \omega_l^B - \omega_e^0 - \frac{\Delta_R}{2} & l = 8, \dots, 16 \\ \omega_l^B - \omega_{i0} - \Delta_{\text{opt}} & l = 17, \dots, 32 \end{cases} \quad (3)$$

Here, the coupling term $\Omega_{\text{st}} = \langle s | (-\mathbf{d} \cdot \mathbf{E}) / \hbar | t \rangle = \Omega_{ts}^*$ is the Rabi frequency, where \mathbf{d} is the electric dipole moment and \mathbf{E} is the electric field of the excitation lights.

First, as the excitation light we consider a circularly polarized σ^+ light with the amplitude of $E(t)$, which propagates along the z axis. The Rabi frequency for σ^+ excitation light is defined as

$$\Omega_{\text{st}}^{\sigma^+} = -\frac{E(t)}{\hbar} d_{FF'} \langle F', m'_F | F, 1, m_F, 1 \rangle. \quad (4)$$

Similarly, for a circularly polarized σ^- light, the Rabi frequency is defined as

$$\Omega_{\text{st}}^{\sigma^-} = -\frac{E(t)}{\hbar} d_{FF'} \langle F', m'_F | F, 1, m_F, -1 \rangle. \quad (5)$$

Here, F and F' are the total angular momenta of $|s\rangle$ and $|t\rangle$, respectively. m_F and m'_F are the magnetic quantum numbers of $|s\rangle$ and $|t\rangle$, respectively. $d_{FF'}$ is the reduced matrix element of the dipole moment operator between levels whose total angular momenta are F and F' , and $\langle F', m'_F | F, 1, m_F, \pm 1 \rangle$ is

the Clebsch-Gordan coefficient. These values for the Cs atom are given in [27].

Next, as the excitation light $\mathbf{E}(t)$, we consider the linearly polarized light with the amplitude of $\mathcal{E}(t)$ whose polarization forms an angle θ with the x axis in the xy plane. The linearly polarized electric field is rewritten by the superposition of two circular polarizations σ^+ and σ^- using the spherical vector basis $\mathbf{e}_{\pm 1} = \mp(\mathbf{e}_x \pm i\mathbf{e}_y)/\sqrt{2}$, as

$$\begin{aligned} \mathbf{E}^{\text{lin}}(t, \theta) &= \mathcal{E}(t)(\mathbf{e}_x \cos \theta + \mathbf{e}_y \sin \theta) \\ &= \frac{\mathcal{E}(t)}{\sqrt{2}} (-e^{-i\theta} \mathbf{e}_{+1} + e^{i\theta} \mathbf{e}_{-1}). \end{aligned} \quad (6)$$

Using Eqs. (4) and (5), the Rabi frequency of the linear polarized light is rewritten as

$$\Omega_{\text{st}}^{\text{lin}} = -\frac{e^{-i\theta}}{\sqrt{2}} \Omega_{\text{st}}^{\sigma^+} + \frac{e^{i\theta}}{\sqrt{2}} \Omega_{\text{st}}^{\sigma^-}. \quad (7)$$

In the CPT resonance, the bichromatic excitation lights of ω_1 and ω_2 interact with two ground hyperfine states and one excited state by a Λ -type scheme. The bichromatic Rabi frequency in this case is also composed of two Rabi frequencies $\Omega_{1\text{st}}[\mathcal{E}_1(t)]$ and $\Omega_{2\text{st}}[\mathcal{E}_2(t)]$, where $\mathcal{E}_1(t)$ and $\mathcal{E}_2(t)$ are the amplitudes of the excitation lights of ω_1 and ω_2 , respectively. Since the detuned frequency component disappears due to the rotating wave approximation, $\Omega_{2\text{st}}(\Omega_{1\text{st}})$ disappears for $s = 1, \dots, 7(8, \dots, 16)$.

Let us assume the direction of the electric field of ω_1 is parallel to the x axis, while that of ω_2 forms an angle θ with the x axis in the xy plane. The coupling term is then written as

$$\Omega_{\text{st}}^{\text{lin}} = \begin{cases} \Omega_{1\text{st}}^{\text{lin}} = -\frac{1}{\sqrt{2}} \Omega_{1\text{st}}^{\sigma^+} + \frac{1}{\sqrt{2}} \Omega_{1\text{st}}^{\sigma^-} & s = 1, \dots, 7 \\ \Omega_{2\text{st}}^{\text{lin}} = -\frac{e^{-i\theta}}{\sqrt{2}} \Omega_{2\text{st}}^{\sigma^+} + \frac{e^{i\theta}}{\sqrt{2}} \Omega_{2\text{st}}^{\sigma^-} & s = 8, \dots, 16 \end{cases} \quad (8)$$

In the Lin \parallel Lin polarization scheme, we adopt $\Omega_{2\text{st}}^{\text{lin}}$ with $\theta = 0$. In the Lin \perp Lin polarization scheme, which corresponds to the push-pull scheme, we adopt $\Omega_{2\text{st}}^{\text{lin}}$ with $\theta = \pi/2$.

The evolution of the atomic system is governed by the Liouville equation, namely, the equation of motion for the density operator $\hat{\rho} = \sum_{l=1}^{32} \sum_{m=1}^{32} \rho_{lm} |l\rangle \langle m|$, as follows:

$$\frac{\partial}{\partial t} \hat{\rho} = -\frac{i}{\hbar} (\hat{H} \hat{\rho} - \hat{\rho} \hat{H}) - \frac{i}{\hbar} (\hat{H}'_{\Gamma} \hat{\rho} + \hat{\rho} \hat{H}'_{\Gamma}) + \hat{\Lambda}, \quad (9)$$

where a non-Hermitian operator \hat{H}'_{Γ} and a source matrix $\hat{\Lambda}$ are added to reflect the relaxation process. \hat{H}'_{Γ} accounts for the decays of atomic states by defining

$$\frac{i}{\hbar} \hat{H}'_{\Gamma} = -\frac{i}{2} \sum_{l=1}^{32} \Gamma_l |l\rangle \langle l| = -\frac{i}{2} \left(\gamma_p \sum_{l=1}^{16} |l\rangle \langle l| + \Gamma \sum_{l=17}^{32} |l\rangle \langle l| \right), \quad (10)$$

where Γ_l is the total decay rate of a sublevel $|l\rangle$ and is a value that depends on several experimental parameters (e.g., the pressure of buffer gas, temperature, and the coating situation of the cell wall). For simplicity, we assume that all excited states have the same decay rate Γ , namely, $\Gamma_l = \Gamma$ for $l = 17, \dots, 32$, which can be estimated from the profile of the absorption spectrum. Similarly, the relaxation rates of all

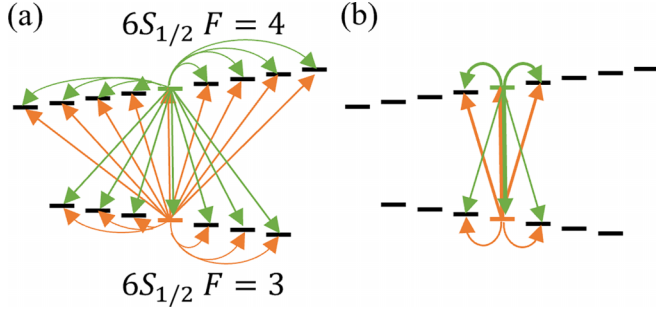


FIG. 2. Schematic diagrams of the relaxation mechanism between ground levels. (a) The uniform relaxation process. (b) The magnetic dipole relaxation process.

ground hyperfine states are assumed to be γ_p , namely, $\Gamma_l = \gamma_p$ for $l = 1, \dots, 16$, which is estimated from the width of the CPT spectrum.

On the other hand, the source matrix $\hat{\Lambda}$ contains nonzero diagonal elements that account for the influx of atoms decaying from other states, as follows:

$$\hat{\Lambda} = \sum_{l=1}^{32} \Lambda_l (\Gamma_1 \rho_{11}, \Gamma_2 \rho_{22}, \dots, \Gamma_{32} \rho_{3232}) |l\rangle \langle l|. \quad (11)$$

Λ_l represents the total influx rate of $|l\rangle$, which is a function of the product of decay rate Γ_m and the population ρ_{mm} of state $|m\rangle$. We ignore the influx rates into the excited states because these are by far smaller than those into the ground states; $\Lambda_l = 0$ for $l = 17, \dots, 32$. We assume that the decay process from an excited state $|n\rangle$ to a ground state $|m\rangle$ is governed by cesium-nitrogen collisions, which would have the dipole-quadrupole interaction, whose decay rates are set to be proportional to the $2/3$ power of the normalized dipole matrix element [28]. As for the relaxation between magnetic sublevels of the ground states, we consider two different processes, depending on the experimental conditions. One is a uniform relaxation process [24] [illustrated in Fig. 2(a)] that is mainly caused by diffusion of Cs atoms, namely collisional relaxation between Cs and wall surfaces, and the replacement of atoms in the optical path with those in thermal equilibrium outside the optical path. The source matrix for the uniform relaxation process $\Lambda_l^{(\text{uni})}$ is written as

$$\Lambda_l^{(\text{uni})} = \sum_{m=1, m \neq l}^{16} \frac{1}{15} \gamma_p^{(\text{uni})} \rho_{mm} + \sum_{n=17}^{32} \frac{T_{nl}^{2/3}}{\sum_{k=1}^{16} T_{nk}^{2/3}} \Gamma \rho_{nn} \quad (12)$$

for $l = 1, \dots, 16$,

where $\gamma_p^{(\text{uni})}$ is the decay rate of a ground state $|m\rangle$ for $m = 1, \dots, 16$. The first and second terms represent the influxes from ground states other than itself and from the excited states, respectively. T_{nl} is the normalized dipole matrix element, which satisfies $\sum_{l=1}^{16} T_{nl}^2 = 1$.

The other relaxation process is caused by the spin-exchange collision between Cs atoms and the collision of Cs atoms with the buffer gas, where the angular momentum of the buffer gas causes a similar action to that of a random

magnetic field on the Cs atoms [29,30]. Here we represent this repopulation process as the magnetic dipole relaxation. The transition distribution in its source matrix $\Lambda_l^{(M1)}$ is proportional to the square of the Clebsch-Gordan coefficient [25]:

$$\Lambda_l^{(M1)} = \sum_{m=1, m \neq l}^{16} \tilde{T}_{nl}^2 \gamma_p^{(M1)} \rho_{mm} + \sum_{n=17}^{32} \frac{T_{nl}^{2/3}}{\sum_{k=1}^{16} T_{nk}^{2/3}} \Gamma \rho_{nn} \quad (13)$$

for $l = 1, \dots, 16$.

Here, $\tilde{T}_{ml}^2 = T_{ml}^2 / (1 - T_{mm}^2)$, which satisfies $\sum_{l=1, l \neq m}^{16} \tilde{T}_{ml}^2 = 1$. It will be necessary to estimate how these processes contribute to the relaxation in the experimental system.

The Liouville equation (9) for each matrix element is written as

$$\frac{\partial}{\partial t} \rho_{lm} = \langle l | \frac{\partial}{\partial t} \hat{\rho} | m \rangle = - \left[\frac{\Gamma_l + \Gamma_m}{2} + i(\delta_l - \delta_m) \right] \rho_{lm} + \frac{i}{2} \sum_{u=1}^{32} (\Omega_{lu} \rho_{um} - \rho_{lu} \Omega_{um}) + \Lambda_l \delta_{lm}, \quad (14)$$

where δ_{lm} is Kronecker's symbol. These equations are rearranged as a vector matrix equation in the form $\frac{\partial}{\partial t} \boldsymbol{\rho} = \mathbf{M} \boldsymbol{\rho}$, where $\boldsymbol{\rho}$ is a vector consisting of 1024 elements of ρ_{lm} and \mathbf{M} is a (1024×1024) matrix consisting of the coefficients of ρ_{lm} generated from the right side of Eq. (14). We developed a computational program to calculate steady-state solutions for ρ_{lm} by equating $\frac{\partial}{\partial t} \boldsymbol{\rho}$ to zero using the condition $\sum_{m=1}^{32} \rho_{mm} = 1$ for a closed atomic system. From Eqs. (11)–(14), Λ_l should be written to satisfy the population conservation, $\sum_{m=1}^{32} \frac{\partial}{\partial t} \rho_{mm} = 0$.

In this calculation of the Liouville equation with a multilevel model, we ignore other sideband lights except for the positive and negative first-order sidebands, and we set $\mathcal{E}_1(t) = \mathcal{E}_2(t) = \mathcal{E}(t)/\sqrt{2}$ for simplicity. At the steady-state condition of Eq. (14), the population of an excited state $|n\rangle$ ($n = 17, \dots, 32$), ρ_{nn} , is written as

$$\rho_{nn} = - \sum_{l=1}^{16} \frac{\text{Im}(\Omega_{nl} \rho_{ln})}{\Gamma_n}. \quad (15)$$

Then, the difference between the sums of the populations of the excited states $\sum_{n=17}^{32} \rho_{nn}$ on resonance and off resonance is proportional to the experimentally observed amplitude of the CPT resonance.

B. Line shape, width, and light shift

We reveal how the formulations for the line shape, width, and light shift of the CPT resonance spectrum are guided from the present multilevel atomic model. Here, we assume that the lower ground level $|g\rangle$ ($g = 1, \dots, 7$) and the upper ground level $|e\rangle$ ($e = 8, \dots, 16$) constitute the CPT resonance. As a necessary condition for CPT resonance to be observed, there exists at least one excited level $|i\rangle$ ($i = 17, \dots, 32$) such that the Rabi frequency determined by the given excitation light is $\Omega_{gi} \neq 0$ and $\Omega_{ei} \neq 0$. Substituting $l = g$ and $m = e$ into Eq. (13), the coherence ρ_{ge} excited between the ground-state

sublevels, $|g\rangle$ and $|e\rangle$, can be written as

$$\left[\frac{\Gamma_g + \Gamma_e}{2} + i(\delta_g - \delta_e) \right] \rho_{ge} = \frac{i}{2} \sum_{u=17}^{32} (\Omega_{gu} \rho_{ue} - \Omega_{eu}^* \rho_{gu}), \quad (16)$$

where u refers to one of the excited levels.

Since $\Gamma_u = \Gamma \gg \Gamma_g$ or Γ_e for any of the excited levels $|u\rangle (u = 17, \dots, 32)$, we define optical decoherence as $\gamma_f = \frac{\Gamma}{2} \cong \frac{\Gamma_u + \Gamma_g}{2} \cong \frac{\Gamma_u + \Gamma_e}{2}$. ρ_{ue} and ρ_{gu} are then written as

$$\begin{aligned} \rho_{ue} &= \frac{i}{2} \frac{\Omega_{gu}^* \rho_{ge} + \sum_{s=1, s \neq g}^{16} \Omega_{su}^* \rho_{se} - \sum_{t=17}^{32} \Omega_{et}^* \rho_{ut}}{\gamma_f + i(\delta_u - \delta_e)}, \\ \rho_{gu} &= \frac{i}{2} \frac{-\Omega_{eu} \rho_{ge} + \sum_{t=17}^{32} \Omega_{gt} \rho_{tu} - \sum_{s=1, s \neq g}^{16} \Omega_{su} \rho_{gs}}{\gamma_f - i(\delta_u - \delta_g)}. \end{aligned} \quad (17)$$

We substitute these into the right-hand side of Eq. (16) and transfer the term containing ρ_{ge} to the left-hand side. Then, ρ_{ge} is solved to be

$$\rho_{ge} = \frac{-\frac{1}{4} \sum_{u=17}^{32} \left[\frac{\Omega_{gu} \left(\sum_{s=1, s \neq g}^{16} \Omega_{su}^* \rho_{se} - \sum_{t=17}^{32} \Omega_{et}^* \rho_{ut} \right)}{\gamma_f + i(\delta_u - \delta_e)} + \frac{\Omega_{eu}^* \left(\sum_{s=1, s \neq g}^{16} \Omega_{su} \rho_{gs} - \sum_{t=17}^{32} \Omega_{gt} \rho_{tu} \right)}{\gamma_f - i(\delta_u - \delta_g)} \right]}{\Delta_{\text{width}} + i(\delta_g - \delta_e - \Delta_{LS})} \quad (18)$$

where

$$\Delta_{\text{width}} = \frac{\Gamma_g + \Gamma_e}{2} + \frac{1}{4} \sum_{u=17}^{32} \left[\frac{|\Omega_{gu}|^2 \gamma_f}{\gamma_f^2 + (\delta_u - \delta_e)^2} + \frac{|\Omega_{ue}|^2 \gamma_f}{\gamma_f^2 + (\delta_u - \delta_g)^2} \right] \quad (19)$$

and

$$\Delta_{LS} = -\frac{1}{4} \sum_{u=17}^{32} \left[\frac{|\Omega_{gu}|^2 (\delta_e - \delta_u)}{\gamma_f^2 + (\delta_u - \delta_e)^2} + \frac{|\Omega_{ue}|^2 (\delta_g - \delta_u)}{\gamma_f^2 + (\delta_u - \delta_g)^2} \right]. \quad (20)$$

By replacing the numerator on the right side of Eq. (18) with C , namely

$$\begin{aligned} C &= -\frac{\gamma_f}{4[\gamma_f^2 + (\Delta_{\text{opt}} + \Delta'_{\text{hfs}}/2)^2]} \left[(\rho_{gg} + \rho_{ee}) + i(\rho_{gg} - \rho_{ee}) \frac{\Delta_{\text{opt}} + \Delta'_{\text{hfs}}/2}{\gamma_f} \right] \sum_{u=17}^{23} \Omega_{gu} \Omega_{eu}^* \\ &\quad - \frac{\gamma_f}{4[\gamma_f^2 + (\Delta_{\text{opt}} - \Delta'_{\text{hfs}}/2)^2]} \left[(\rho_{gg} + \rho_{ee}) + i(\rho_{gg} - \rho_{ee}) \frac{\Delta_{\text{opt}} - \Delta'_{\text{hfs}}/2}{\gamma_f} \right] \sum_{u=24}^{32} \Omega_{gu} \Omega_{eu}^*, \end{aligned} \quad (21)$$

the real part of ρ_{ge} , $\text{Re}(\rho_{ge})$, which determines the shape of the CPT resonance curve in the case where $\Omega_1 \Omega_2$ is a real number, becomes

$$\text{Re}(\rho_{ge}) = -\frac{\text{Re}(C) \Delta_{\text{width}}}{\Delta_{\text{width}}^2 + (\delta_g - \delta_e - \Delta_{LS})^2} + \frac{\text{Im}(C) (\delta_g - \delta_e - \Delta_{LS})}{\Delta_{\text{width}}^2 + (\delta_g - \delta_e - \Delta_{LS})^2}. \quad (22)$$

Here, $\text{Re}(C)$ and $\text{Im}(C)$ are the real part and the imaginary part of C . The line shape of the CPT resonance as a function of $\delta_g - \delta_e$ is composed of the sum of the symmetric Lorentzian function (first term) and the antisymmetric Lorentzian function (second term), with the width Δ_{width} and the light shift Δ_{LS} . This line shape matches that obtained for the three-level model, except for their amplitudes [$\text{Re}(C)$ and $\text{Im}(C)$]. Thus, we can derive the line shape, width, and light shift of the CPT resonance for the multilevel atomic model. Equation (21) is the simplified form of C in a condition where CPT resonance frequencies are resolved clearly by the magnetic field and the frequencies of the excitation lights are tuned to the excited state $6P_{1/2} F' = 3$ or 4. Note that the term $\Delta_{\text{opt}} + \Delta'_{\text{hfs}}/2$ (or $\Delta_{\text{opt}} - \Delta'_{\text{hfs}}/2$) is nearly zero when the excitation lights are

tuned to $F' = 3$ (or 4) levels. When the excitation lights are detuned, asymmetry in the CPT spectrum appears, as reported in [21,22,31,32]. A rigorous derivation of the CPT spectrum in the 32-level model is presented in the Appendix.

III. EXPERIMENTAL SETUP

The experimental setup is shown in Fig. 3, which is nearly identical to the one described in our previous paper [20]. Magnetic materials were carefully removed from the vicinity of the cell to reduce the inhomogeneous magnetic field and the width of the magnetic-field-sensitive CPT resonance. The residual inhomogeneity of the magnetic field is estimated to be less than 0.3 μT . We utilized three Cs-vapor cells filled with

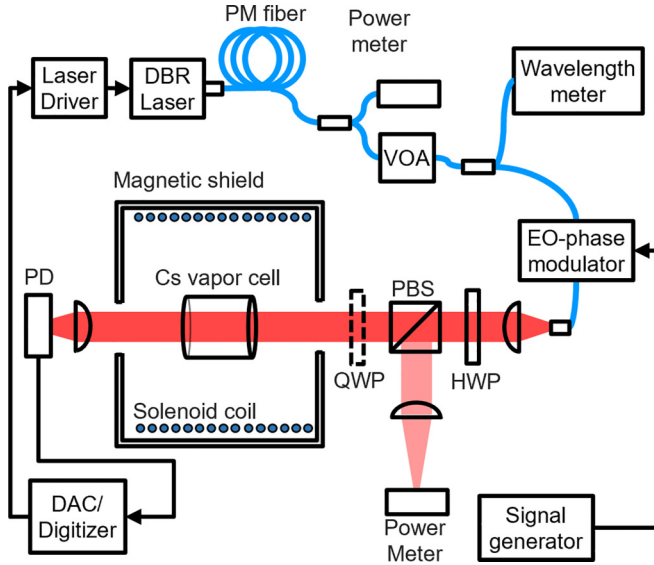


FIG. 3. Experimental setup. VOA, variable optical attenuator; HWP, half-wave plate; PBS, polarizing beam splitter; QWP, quarter-wave plate; PD, photodetector.

different pressures of nitrogen buffer gas. The Cs-vapor cells were used at room temperature and not actively controlled by heating devices. The buffer gas pressure for each cell was determined from the measured value of the CPT resonance frequency shift based on the reported value of the buffer gas shift [33]. The length of the cells was 25 mm. The pressure and shape of used Cs-vapor cells are listed in Table I, together with the decay rate of the ground states γ_p and the excited-state relaxation rate Γ , whose values are necessary to calculate the CPT resonance. γ_p was determined experimentally from the CPT resonance width when the excitation light intensity is close to zero (see Sec. IV D). We also estimated γ_p from Eqs. (3.5.6) and (3.6.98) in Ref. [30] using the pressure of the buffer gas, the configuration of the cell, the diffusion coefficient, and temperature. We confirmed that the estimated values of γ_p were consistent with experimental values in the order of magnitudes. The excited-state relaxation rate Γ was determined from the width (full width at half maximum) of the absorption spectrum, which results from the convolution of collision broadening and Doppler broadening [34]. The width of the Doppler broadening at room temperature is about

TABLE I. The pressure and shape of the gas cells used in the present experiments with the decay rate of the ground states γ_p and the decay rate of the excited states Γ , which are determined experimentally. The length of the cells is 25 mm. Uncertainties are given by a standard deviation.

Parameter	Cell 1	Cell 2	Cell 3
N ₂ pressure (kPa)	0.09 ± 0.01	1.35 ± 0.05	11.5 ± 0.4
Shape	Square	Circle	Square
Cross section	$20 \times 20 \text{ mm}^2$	10-mm radius	$20 \times 20 \text{ mm}^2$
$\gamma_p/2\pi$ (kHz)	24.5 ± 0.8	0.107 ± 0.006	0.081 ± 0.006
$\Gamma/2\pi$ (GHz)	0.38 ± 0.03	0.51 ± 0.03	1.69 ± 0.18

360 MHz. In the present paper, uncertainties are given by a standard deviation.

The Cs Cell was irradiated by a distributed Bragg reflector laser beam, whose wavelength was tuned to the vicinity of transition from $6S_{1/2}$ to $6P_{1/2}F' = 3$ or 4 in the D_1 line of ^{133}Cs . The laser light was modulated by an electro-optic modulator driven with a modulation frequency f_m set to around one-half of the hyperfine frequency splitting. The positive first-order and negative first-order sideband frequencies were used as bichromatic excitation lights ω_1 and ω_2 , whose intensities are identical. The polarization of excitation light was changed to circular polarization or linear polarization using a quarter-wave plate. The frequency-modulated light was expanded to be a 7.2-mm-diameter beam at the center of a Cs-vapor cell and passed through the cell. The intensity of laser beam used in this experiment was less than $15 \mu\text{W}/\text{mm}^2$, which is at most 20% of the saturation intensity of the D_1 line [27].

The spectrum, amplitude, and width of the CPT resonance were measured as a function of detuning frequency, which is the difference from the center modulation frequency of the (0,0) resonance. The measured CPT amplitudes were defined by the difference of the transmitted beam intensity between on resonance (peak) and far-off resonance in $\mu\text{W}/\text{mm}^2$, which are compared to the CPT amplitude calculated using Eq. (15) with the experimental values of γ_p and Γ .

IV. RESULTS AND DISCUSSION

A. Dependence of the CPT spectrum on buffer-gas pressures

Figures 4(a)–4(c) show the experimental CPT spectra observed in three gas cells with different buffer gas pressures of 0.09, 1.35, and 11.5 kPa excited by circular polarization tuned to $F' = 4$ levels. These are spectra with seven Zeeman peaks, which correspond to the (m, m) resonance between two ground levels of $|F = 3, m_F = m\rangle$ and $|4, m\rangle$ from $m = -3$ to $+3$, respectively. The experimental results show how greatly the width and the peak amplitude pattern of the CPT resonance vary with the gas pressure of the cell. Some experimental spectra show an asymmetric feature, because the scan speed of the frequency is too fast. In cells with higher buffer gas pressure, the width of the CPT resonance becomes narrower. As for the amplitude distribution of the CPT spectra, the CPT resonance of $(-3, -3)$ in the high-pressure cell becomes more significant, which may suggest that the population distribution among the ground states is different depending on the buffer gas pressure.

Warren *et al.* calculated the CPT spectrum of ^{87}Rb vapor with 10-Torr (1.3-kPa) Ne buffer gas at 53°C using “the uniform relaxation” represented in Eq. (12) as a source matrix [23]. In a different approach, Matsuda *et al.* calculated the CPT spectrum of ^{133}Cs vapor with 10-kPa Ne-Ar buffer gas at 80°C using “the magnetic dipole relaxation” represented in Eq. (13) [25]. The two relaxations are illustrated in Fig. 2. Here we show that such a difference in the intensity distribution will be explained by a ratio of the combination of the two relaxation processes. We assume that the relaxation rate of the ground states γ_p is the sum of the relaxation rates of the two processes $\gamma_p^{(\text{uni})}$ and $\gamma_p^{(M1)}$, namely, $\gamma_p = \gamma_p^{(\text{uni})} + \gamma_p^{(M1)}$.

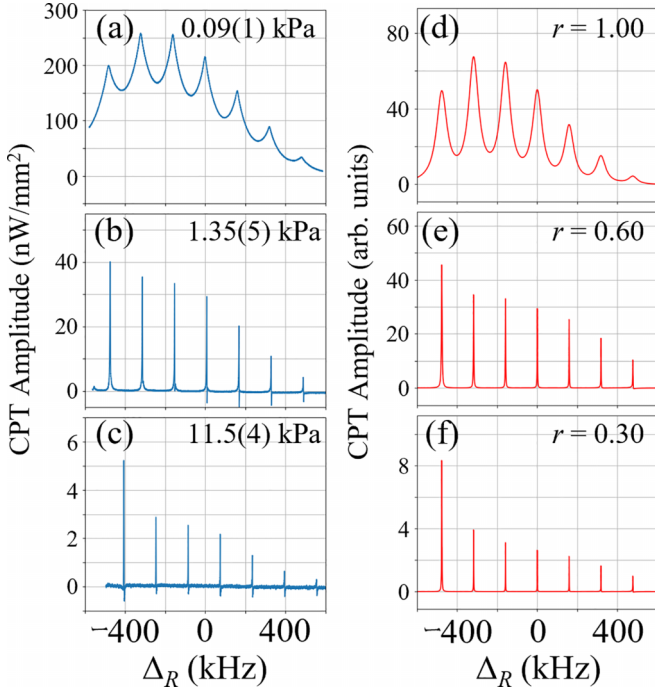


FIG. 4. Zeeman CPT spectra excited with circularly polarized lights $\sigma^- - \sigma^-$ tuned to the $F' = 4$ levels at $B = 22.7 \mu\text{T}$ observed in three cells at different N_2 pressures. The excitation intensities are $I_1 = I_2 = 6.6 \mu\text{W}/\text{mm}^2$. The scan speed of the frequency was 600 kHz/s. (a)–(c) Experimental spectra in (a) cell 1, 0.09 kPa; (b) cell 2, 1.35 kPa; and (c) cell 3, 11.5 kPa. (d)–(f) Calculated spectra with the corresponding parameters for each gas cell of (d) cell 1, (e) cell 2, and (f) cell 3. r is the ratio of the uniform relaxation to the total relaxation.

If we define the ratio of the uniform relaxation to the total relaxation as r , the ratio of the magnetic dipole relaxation is $(1-r)\gamma_p$. Then, the source matrix for the total relaxation process is written as follows:

$$\Lambda_l^{(\text{uni}+M1)} = \sum_{m=1, m \neq l}^{16} \left[\frac{1}{15} r + \tilde{T}_{nl}^2 (1-r) \right] \gamma_p \rho_{mm} + \sum_{n=17}^{32} \frac{T_{nl}^{2/3}}{\sum_{k=1}^{16} T_{nk}^{2/3}} \Gamma \rho_{nn} \quad \text{for } l = 1, \dots, 16. \quad (23)$$

As stated in Sec. III, the values of γ_p and Γ in Table I were determined experimentally from the CPT spectra and the absorption spectra measured for each cell, respectively. Substituting Eq. (23) into Eq. (14), we calculated the Zeeman CPT spectrum for each cell so as to fit to the experimental results by changing r as a fitting parameter. Figures 4(d)–4(f) show the CPT spectra calculated using $r = 1.00$, 0.60, and 0.30 for the buffer gas pressures of 0.09, 1.35, and 11.5 kPa, respectively. The magnitude of the CPT amplitude for calculation is defined so that the CPT amplitude of the (0,0) resonance for 1.35 kPa is equal to the experimental one. Note that the buffer gas shift, which is clearly seen in cell 3, is not included in the present calculation. The three calculated amplitude patterns of the CPT spectrum nearly reproduce

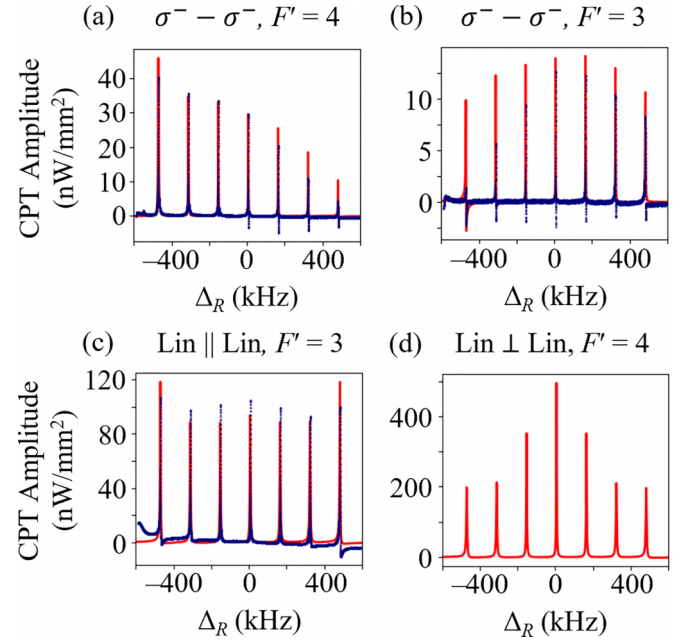


FIG. 5. Zeeman CPT spectra in cell 2 at $B = 22.7 \mu\text{T}$. N_2 pressure is 1.35 kPa (cell 2), and the excitation intensities are $I_1 = I_2 = 6.6 \mu\text{W}/\text{mm}^2$. The scan speed of the frequency was 600 kHz/s. (a), (b) Experimental [blue (gray dot) and calculated [red (light gray) line] CPT spectra excited with circularly polarized light $\sigma^- - \sigma^-$ tuned to (a) $F' = 4$ and (b) $F' = 3$ levels. (c) CPT spectra excited with Lin || Lin schemes tuned to $F' = 3$ level. (d) Lin \perp Lin scheme tuned to $F' = 4$ level. Calculations are executed with $r = 0.6$, $\Gamma/2\pi = 0.51 \text{ GHz}$, and $\gamma_p/2\pi = 0.107 \text{ kHz}$ at $B = 139 \mu\text{T}$. The amplitude of the calculated (0,0) CPT resonance excited with circularly polarized light $\sigma^- - \sigma^-$ tuned to $F' = 4$ is normalized to the experimental one.

those for the corresponding experimental ones, although the calculated spectrum width for cell 1 is somewhat narrower than the experimental width. Thus, the linewidth of CPT resonance irradiated at a few $\mu\text{W}/\text{mm}^2$ becomes wider as Γ is smaller. In the present calculation using the multilevel model, the calculated amplitude pattern was able to reproduce the experimental pattern in each cell, but relative amplitudes between different cells are somewhat different between them. In order to discuss this more precisely, it will be necessary to consider the shape of the cell and the variation along the length of the cell.

B. First-order Zeeman CPT spectrum

In the rest of this paper, we will discuss CPT spectrum for cell 2 (1.35 kPa). First, we study how the patterns of the Zeeman CPT spectra are related to the excitation level of $F' = 3$ or 4 and the polarization scheme of the excitation lights. In Fig. 5, blue dots indicate the observed CPT spectra and red solid lines indicate the calculated correspondent spectra for $r = 0.6$. Then, the calculated peak amplitude of the (0, 0) resonance excited with circularly polarized lights $\sigma^- - \sigma^-$ whose frequencies are tuned to $F' = 4$ is defined as being equal to the experimental one, as shown in Fig. 5(a). Figures 5(a) and 5(b) show the CPT spectra excited by $\sigma^- - \sigma^-$

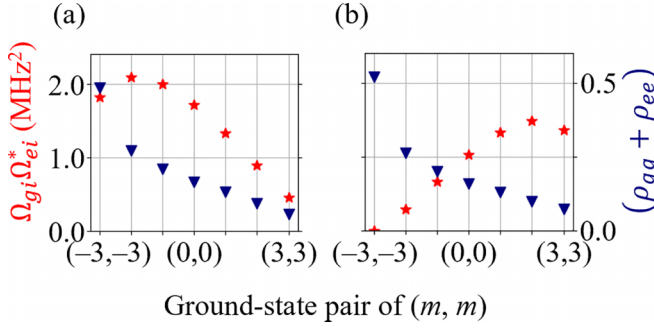


FIG. 6. The population of two ground states [blue (gray) triangle] and the product of Rabi frequencies [red (light gray) star] for the CPT resonance tuned to (a) $F' = 4$ and (b) $F' = 3$ levels. The indices g , e , and i in the product of Rabi frequencies indicate the two ground levels and the excited level of the corresponding Λ transition.

tuned to $F' = 4$ and 3, respectively. The $(-3, -3)$ resonance in Fig. 5(a) produces the largest signal. In contrast, a roughly antisymmetric pattern is observed in Fig. 5(b), where the $(0, 0)$ resonance is the largest, and the (m, m) resonance with a positive value of m is larger than that with a negative value. We find the patterns obtained by calculation fairly match the experimental patterns, except that the observed $(-m, -m)$ resonances become smaller than the calculated results as the value of m increases. This is presumably due to the spatial inhomogeneity of the magnetic field in the experimental system.

The amplitude of the Zeeman CPT spectra is determined by the sum of populations of the ground states related to the CPT resonance, and the product of two Rabi frequencies corresponding to the Λ scheme, as shown in Eq. (21). For each resonance signal excited to $F' = 4$ and 3 levels, the former and latter are respectively shown by blue triangles and red stars in Figs. 6(a) and 6(b). Though the distribution of the sum of the populations is similar regardless of $F' = 4$ and 3 levels, the pattern of the product of Rabi frequencies is different for the two excitations depending on the values of their Clebsch-Gordan coefficients. Here, we note that the $(-3, -3)$ resonance excited to $F' = 3$ is observed in both the numerical and experimental results even though the product of the Rabi frequencies is zero, which is due to the contribution from the detuned excitation to $F' = 4$ levels.

We also calculated the Zeeman CPT spectra excited with the Lin \parallel Lin polarization scheme to $F' = 3$ levels, and with the Lin \perp Lin polarization scheme to $F' = 4$ levels. They are shown by red solid lines in Figs. 5(c) and 5(d), respectively, with relative values to the calculated peak amplitude of the $(0, 0)$ resonance excited by $\sigma^- - \sigma^-$ tuned to $F' = 4$. In Fig. 5(c), the present experimental result is also overlaid with blue dots.

The calculated pattern is almost identical to that observed experimentally. The pattern of Fig. 5(d) was already shown by the experiment with the push-pull optical pumping [17]. We summarize the measured and calculated peak amplitudes of the CPT resonance excited with different schemes in Table II. The calculated ratios are in fairly good agreement with the experimental ratios. We confirm using the present multilevel model that the Lin \perp Lin polarization scheme produces the largest amplitude of the $(0, 0)$ CPT resonance in the D_1 transition of ^{133}Cs atoms.

C. Second-order Zeeman CPT spectrum

Depending on the strength of the quantized magnetic field, each Zeeman CPT spectrum is split into three Λ -scheme resonances of (m, m) , $(m-1, m+1)$, and $(m+1, m-1)$ due to the second-order Zeeman effect. The resonances of $(m-1, m+1)$ and $(m+1, m-1)$ via $m'_F = m$ are created by the excitation scheme of the linear-linear polarization, whereas the (m, m) resonance is created by two σ^+ polarizations via $m'_F = m+1$, or two σ^- polarizations via $m'_F = m-1$. For such a double- Λ scheme of the (m, m) resonance generated by the linear-linear polarization, Liu *et al.* derived the condition where a dark state common to the two Λ schemes exists [17], as follows:

$$e^{2i\theta} = \frac{\Omega_{2s't}^{\sigma^+} \Omega_{1st'}^{\sigma^-}}{\Omega_{1st}^{\sigma^+} \Omega_{2s't'}^{\sigma^-}}. \quad (24)$$

Here, we define level $|s\rangle$ as $F = 3$ and $m_F = m$, $|s'\rangle$ as $F = 4$ and $m_F = m$, $|t\rangle$ as $F' = 3$ and $m_F = m+1$, and $|t'\rangle$ as $F' = 3$ and $m_F = m-1$. θ is the angle between two electric fields.

Conversely, when the dark state for a transition is the bright state for the other transition, the two Λ schemes act to weaken each other. The condition is as follows:

$$e^{2i\theta} = -\frac{\Omega_{1st}^{\sigma^+} \Omega_{1st'}^{\sigma^-}}{\Omega_{2s't}^{\sigma^+} \Omega_{2s't'}^{\sigma^-}}. \quad (25)$$

In the case of $m = 0$ in the D_1 transition of ^{133}Cs , Eq. (24) becomes $e^{2i\theta} = -1$. Therefore, in the Lin \perp Lin (or push-pull) scheme with $\theta = \pi/2$, a common dark state exists and the $(0, 0)$ CPT resonance occurs, along with $(-1, 1)$ and $(1, -1)$ [17]. In contrast, in the Lin \parallel Lin scheme with $\theta = 0$, no $(0, 0)$ CPT resonance occurs, since the dark state for one Λ scheme becomes the bright state for the other. Note that in the case of $m \neq 0$, Eq. (25) is still satisfied in the Lin \parallel Lin scheme with $\theta = 0$ and $E_1 = E_2$.

We measured in precisely the second-order Zeeman splitting of seven CPT resonances [Fig. 5(c)] observed in the Lin \parallel Lin scheme. The blue dots in Fig. 7 indicate experimental spectra in the vicinity of the (m, m) resonances for

TABLE II. The amplitude ratio of the CPT resonances excited with different schemes at $I_1 = I_2 = 6.6 \mu\text{W}/\text{mm}^2$.

Parameter	$\sigma^- - \sigma^-$	$\sigma^- - \sigma^-$	Lin \parallel Lin	Lin \perp Lin
Excitation levels	$F' = 4$	$F' = 3$	$F' = 3$	$F' = 4$
CPT resonance	$(0, 0)$	$(0, 0)$	$(-1, 1)$ and $(1, -1)$	$(0, 0)$
Relative amplitude of experiment	1.0	0.44	3.6	
Relative amplitude of calculation	1.0	0.47	3.2	17

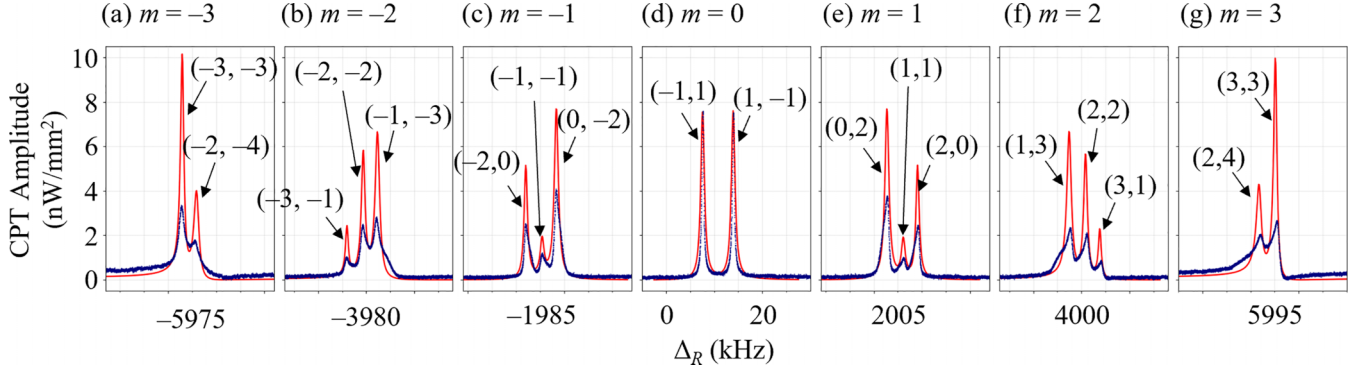


FIG. 7. Calculated [red (light gray) line] and experimental [navy (gray) dot] CPT spectra in cell 2 near the (m, m) resonance for $m = -3, \dots, +3$, by Lin \parallel Lin excitation tuned to $F' = 3$ levels at $B = 285 \mu\text{T}$. The excitation intensities are $I_1 = I_2 = 1.2 \mu\text{W}/\text{mm}^2$. The scan speed of the frequency was 80 kHz/s . Calculations are executed with $r = 0.6$, $\Gamma/2\pi = 0.51 \text{ GHz}$, and $\gamma_p/2\pi = 0.107 \text{ kHz}$. The amplitude of the calculated CPT spectra are shown with the normalization so that the calculated peak amplitude of the $(-1, 1)$ resonance is identical to the experimental one.

$m = -3, \dots, +3$ excited to $F' = 3$ levels with the Lin \parallel Lin polarization. Except for $m = 0$, we can clearly observe the (m, m) resonances. The amplitude of the (m, m) resonance increases as the absolute value of m increases. We also calculated the CPT spectrum using the multilevel model with the normalization so that the calculated peak amplitude of the $(-1, 1)$ resonance is identical to the experimental one. The calculated signal is overlaid by red solid lines in Fig. 7, and we find that spectra of the $(-1, 1)$ and $(1, -1)$ resonances agree fairly well with the experimental ones. As the value of m increases, the peak amplitude in the experimental spectra becomes smaller than the calculated ones. As we already stated, it occurs due to the inhomogeneity of the magnetic

field, which is estimated to be less than $0.3 \mu\text{T}$. Furthermore, we confirm that the (m, m) resonances, except for $m = 0$, occur in the calculated spectrum. The fact that the (m, m) resonance except for $m = 0$ is not forbidden in experiment and calculation suggests that an additional condition is required in the double- Λ scheme to suppress the (m, m) resonance. We explain this as follows.

As written in Eq. (15), a measure of transparency is $\sum_{n=17}^{32} \sum_{l=1}^{16} \text{Im}(\Omega_{nl} \rho_{ln})$. Here, we consider a double- Λ scheme composed of the ground-state pair, $|g\rangle$ and $|e\rangle$, and the excited states associated with σ^+ and σ^- polarizations, $|n^+\rangle$ and $|n^-\rangle$. The contribution of this double- Λ scheme to transmittance is given by the following:

$$\begin{aligned} \text{Im}(\Omega_{n^+g} \rho_{gn^+} + \Omega_{n^-g} \rho_{gn^-}) &= \text{Im} \left[i\Omega_{n^+g} \frac{\sum_{v=17}^{32} \Omega_{gv} \rho_{vn^+} - \sum_{u=1}^{16} \Omega_{un^+} \rho_{gu}}{\Gamma_g + \Gamma_{n^+} + 2i(\delta_g - \delta_{n^+})} + i\Omega_{n^-g} \frac{\sum_{v=17}^{32} \Omega_{gv} \rho_{vn^-} - \sum_{u=1}^{16} \Omega_{un^-} \rho_{gu}}{\Gamma_g + \Gamma_{n^-} + 2i(\delta_g - \delta_{n^-})} \right] \\ &\cong -\frac{1}{4\gamma_f} \{ (|\Omega_{gn^+}|^2 + |\Omega_{gn^-}|^2) \rho_{gg} + \text{Re}[(\Omega_{gn^+}^* \Omega_{en^+} + \Omega_{gn^-}^* \Omega_{en^-}) \rho_{ge}] \}. \end{aligned} \quad (26)$$

Here, we assume the frequencies of the excitation lights are tuned to both the n^+ and n^- levels, such that $|\delta_g - \delta_{n^\pm}| \ll \gamma_f$. Similarly,

$$\text{Im}(\Omega_{n^+e} \rho_{en^+} + \Omega_{n^-e} \rho_{en^-}) \cong -\frac{1}{4\gamma_f} \{ (|\Omega_{en^+}|^2 + |\Omega_{en^-}|^2) \rho_{ee} + \text{Re}[(\Omega_{gn^+}^* \Omega_{en^+} + \Omega_{gn^-}^* \Omega_{en^-}) \rho_{ge}] \}. \quad (27)$$

The term associated with ρ_{gg} or ρ_{ee} is the contribution of one-photon absorption. From Eqs. (21) and (22), the term associated with ρ_{ge} is written as follows:

$$\begin{aligned} \text{Re}[(\Omega_{gn^+}^* \Omega_{en^+} + \Omega_{gn^-}^* \Omega_{en^-}) \rho_{ge}] &= \frac{\text{Re}[(\Omega_{gn^+}^* \Omega_{en^+} + \Omega_{gn^-}^* \Omega_{en^-}) \mathcal{C}] \Delta_{\text{width}}}{\Delta_{\text{width}}^2 + (\delta_g - \delta_e - \Delta_{LS})^2} + \frac{\text{Im}[(\Omega_{gn^+}^* \Omega_{en^+} + \Omega_{gn^-}^* \Omega_{en^-}) \mathcal{C}] (\delta_g - \delta_e - \Delta_{LS})}{\Delta_{\text{width}}^2 + (\delta_g - \delta_e - \Delta_{LS})^2} \\ &\cong -\frac{\rho_{gg} + \rho_{ee}}{4\gamma_f} \frac{\Delta_{\text{width}}}{\Delta_{\text{width}}^2 + (\delta_g - \delta_e - \Delta_{LS})^2} |\Omega_{gn^+}^* \Omega_{en^+} + \Omega_{gn^-}^* \Omega_{en^-}|^2. \end{aligned} \quad (28)$$

Therefore, the amplitude of the CPT resonance depends on the square of $\Omega_{gn^+}^* \Omega_{en^+} + \Omega_{gn^-}^* \Omega_{en^-} \equiv \Omega_{1st}^{\sigma^+} \Omega_{2st}^{*\sigma^+} + \Omega_{1st'}^{\sigma^-} \Omega_{2st'}^{*\sigma^-}$. This value is zero for $m = 0$ but is proportional to 0.0065, 0.021, and 0.027 for $m = \pm 1, \pm 2, \pm 3$, respectively. Thus,

in order to prohibit the (m, m) CPT resonance excited to $F' = 3$ levels with the linear-linear polarization in case of the double- Λ scheme, $\sum_{u=17}^{23} \Omega_{gu} \Omega_{eu}^* = 0$ is required in addition to the conditions of $\theta = 0$ and $\mathcal{E}_1 = \mathcal{E}_2$. This condition is

equivalent to

$$\Omega_{1st}^{\sigma+} \Omega_{2s't}^{*\sigma+} = -\Omega_{1st'}^{\sigma-} \Omega_{2s't'}^{*\sigma-}. \quad (29)$$

D. Dependence of CPT resonance on excitation intensity

In our previous paper [20], we showed that the amplitude of the $(-1, 1)$ and $(1, -1)$ resonances excited with the Lin || Lin polarization increases approximately in proportion to the excitation intensity, while the amplitude of the $(0, 0)$ resonance excited with $\sigma^- - \sigma^-$ polarization moderately saturates. We concluded that the former can be described by the simple three-level model and the latter by the four-level model with a trap state. However, such behaviors should be explained by one complete equation that considers all sublevels related to the D_1 line of ^{133}Cs . In this section, we compare the experimental results of the dependency of the $(-1, 1)$ and the $(0, 0)$ resonances on excitation intensity with the calculated ones using the present multilevel model.

The width and the amplitude of the $(0, 0)$ resonance excited with $\sigma^- - \sigma^-$ polarization tuned to $F' = 3$ and 4 levels and those of the $(-1, 1)$ resonance excited with the Lin || Lin polarization tuned to $F' = 3$ and 4 levels were measured for cell 2 (N_2 : 1.35 kPa) and plotted as a function of the excitation intensity in Fig. 8, by green (light gray) circles, blue (gray) squares, red (light gray) triangles, and magenta (gray) stars, respectively. Figure 8(a) shows the measured widths of those resonances as a function of the excitation intensity, together with the calculated widths using the multilevel model with the values of $\Gamma/2\pi = 0.51$ GHz and $\gamma_p/2\pi = 0.107$ kHz. The pink (light gray) shaded area of the calculated width for excitation with the Lin || Lin polarization tuned to $F' = 3$ shows the uncertainty of $\pm 4\%$. The calculated widths for excitation with the Lin || Lin polarization are in good agreement with the experimental widths. This fact was already ascertained in the spectra of the $(-1, 1)$ and $(1, -1)$ resonance of Fig. 7(d). On the other hand, the calculated widths for excitation with the $\sigma^- - \sigma^-$ polarization are wider than the experimental width by three times the uncertainty; however, the tendency of the width against the excitation intensity is similar. It is found that the width excited by the Lin || Lin polarization is wider than that excited by the $\sigma^- - \sigma^-$ polarization and the width excited to $F' = 4$ is wider than that excited to $F' = 3$. According to Eq. (19), the width of CPT resonance becomes γ_p at the excitation intensity of almost zero, but it increases approximately with the slope due to the reciprocal of Γ as intensity increases, as stated in Sec. IV A. Thus, the experimental decay rate of the ground states $\gamma_p/2\pi = 0.107 \pm 0.006$ kHz was obtained from the CPT resonance width when the excitation light intensity is close to zero.

Figure 8(b) shows the comparison of the experimental and calculated amplitudes of CPT resonance. The amplitudes excited by the Lin || Lin polarization tuned to $F' = 3$ and 4 increase proportionally with intensity, as shown by red (light gray) triangles and magenta (gray) stars, respectively. The magnitude of the experimental CPT amplitude is on the order of nW/mm² for incident light of a few $\mu\text{W}/\text{mm}^2$. The calculated amplitude excited with the Lin || Lin scheme to $F' = 3$ is fitted to the experimental one, and as shown in red line agrees quite well with the experimental values within the uncertainty

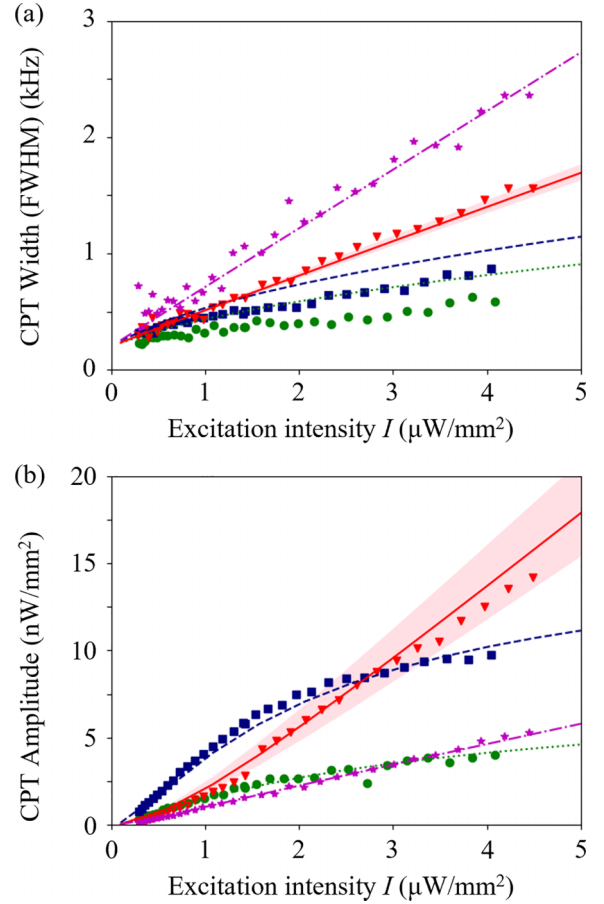


FIG. 8. Measured and calculated widths and amplitudes of the $(0, 0)$ or $(-1, 1)$ resonance for different polarization and excitation levels as a function of the excitation intensity I at $B = 139$ μT . The scan speed of the frequency was 100 kHz/s. N_2 pressure is 1.35 kPa (cell 2). Calculations are executed with $r = 0.6$, $\Gamma/2\pi = 0.51$ GHz, and $\gamma_p/2\pi = 0.107$ kHz. (a), (b) The widths (a) and intensities (b) of the CPT resonances as a function of the excitation intensity. The calculated amplitude excited with the $\sigma^- - \sigma^-$ scheme is normalized to the experimentally measured amplitude tuned to $F' = 4$ levels, while the calculated amplitude excited with the Lin || Lin scheme is normalized to the experimentally measured amplitude tuned to $F' = 3$ levels. Green (light gray) circle (measured) and dotted line (calculated): The $(0, 0)$ resonance excited with the $\sigma^- - \sigma^-$ scheme tuned to $F' = 3$ levels. Blue (gray) square (measured) and dashed line (calculated): The $(0, 0)$ resonance excited with the $\sigma^- - \sigma^-$ scheme tuned to $F' = 4$ levels. Red (light gray) triangle (measured) and solid line (calculated): The $(-1, 1)$ resonance excited with the Lin || Lin scheme tuned to $F' = 3$ levels. Magenta (gray) star (measured) and dash-dot line (calculated): The $(-1, 1)$ resonance excited with the Lin || Lin scheme tuned to $F' = 4$ levels.

($\pm 20\%$) of the calculated amplitude, which are shown by the pink (light gray) and shaded area. Then the calculated amplitude excited by the Lin || Lin scheme to $F' = 4$ in magenta line agrees with the experimental values similarly. Contrary to this, the calculated amplitude excited with the $\sigma^- - \sigma^-$ scheme was about twice the calculated amplitudes excited with the Lin || Lin scheme. Therefore, the calculated amplitude excited with the $\sigma^- - \sigma^-$ scheme to $F' = 4$ is also fitted to the measurement data, as shown in blue line. Then, we confirm that the

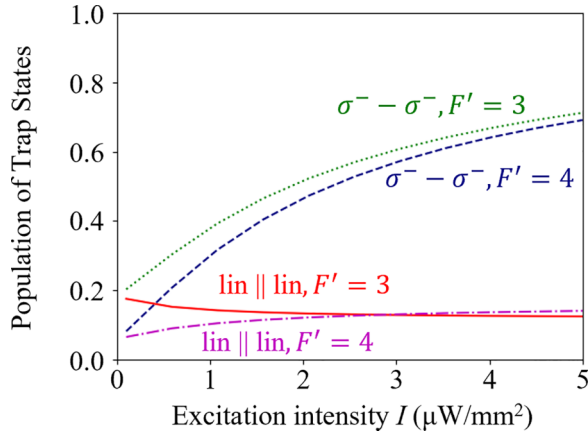


FIG. 9. The calculated population of trap states for several excitation schemes as a function of excitation intensity. Calculations are executed with $r = 0.6$, $\Gamma/2\pi = 0.51$ GHz, and $\gamma_p/2\pi = 0.107$ kHz at $B = 139$ μ T, which are optimal values for cell 2. Green (light gray) dotted line: The $(0, 0)$ resonance excited with the $\sigma^- - \sigma^-$ scheme tuned to $F' = 3$ levels. Blue (gray) dashed line: The $(0, 0)$ resonance excited with the $\sigma^- - \sigma^-$ scheme tuned to $F' = 4$ levels. Red (light gray) solid line: The $(-1, 1)$ resonance excited with the Lin || Lin scheme tuned to $F' = 3$ levels. Magenta (gray) dash-dot line: The $(-1, 1)$ resonance excited with the Lin || Lin scheme tuned to $F' = 4$ levels.

relative relationships between $F' = 4$ and 3 are in good agreement with the experimental values. Similar to our previous results [20], the amplitude of the CPT resonance excited with $\sigma^- - \sigma^-$ polarization saturates as excitation intensity increases. On the other hand, that excited with Lin || Lin polarization is increasing in proportion to the excitation intensity because the excitation intensity is less than the saturation intensity of the D_1 line. For reference, we note that the absorbed intensity of a cell irradiated at $I = 2.5$ μ W/mm² was 0.24 and 0.36 μ W/mm² for excitation by the $\sigma^- - \sigma^-$ polarization tuned to $F' = 4$ and by the Lin || Lin polarization tuned to $F' = 3$, respectively.

To investigate the difference between dependencies on the excitation intensity for $\sigma^- - \sigma^-$ excitation and Lin || Lin excitation, we calculated the population of trap states using the 32-level model. The state $|8\rangle$ in Fig. 1 is a trap state for the excitation to $F' = 4$ levels, and states $|1\rangle$, $|8\rangle$, and $|9\rangle$ are trap states for the excitation to $F' = 3$ levels. The populations of the trap states for several excitation schemes are shown in Fig. 9 as a function of the excitation intensity. In the case of no excitation light, the populations of the ground states are thermally equivalent, namely the population of the trap state is 19% for $F' = 3$ and 6.3% for $F' = 4$. For $\sigma^- - \sigma^-$ excitation, the population of the trap state increases as the intensity increases and reaches 60% at more than 3 μ W/mm². In contrast, that for Lin || Lin excitation does not depend on the excitation intensity and is almost constant. These findings clarify that the CPT amplitude for $\sigma^- - \sigma^-$ excitation saturates while the CPT amplitude for the Lin || Lin excitation increases in proportion to the excitation intensity. The population of the trap state for the Lin \perp Lin excitation to $F' = 4$ levels versus excitation intensity is almost the same as that for Lin || Lin excitation to the $F' = 4$ levels. The reason why the

calculated CPT amplitude for $\sigma^- - \sigma^-$ excitation deviates from the experimental one to some extent may be that it reflects the real population of the trap state.

Thus, the phenomena explained separately using the separate equations of a three-level system and four-level system in the previous paper can be explained uniformly by calculation using the equations of the multilevel model. As stated above, many phenomena can be calculated using the present multilevel model. However, there is not a complete agreement between the experimental data and the calculated results using the present model. There are several things that need to be considered for improvement. It would be necessary to add spatial characteristics that reflect the Gaussian intensity distribution of the excitation light, the attenuation of light in the thickness direction of the gas cell, the saturation effect of the light, the spatial nonuniformity of the magnetic field, and so on. Although we used a frequency-modulated light for the excitation of Cs atoms in the present experiment, we took into consideration the positive first sideband and the negative first sideband frequencies as bichromatic light in the present model. More precisely, the interactions with a carrier frequency and other higher-order sideband frequencies should be included in the model.

V. CONCLUSION

We constructed a computational multilevel atomic model of the Liouville density-matrix equation to investigate the CPT resonances excited by the bichromatic lights of various excitation schemes between the ground hyperfine levels. The model contains 32 Zeeman sublevels on the D_1 line of ^{133}Cs atoms. We also derived formulations for the line shape, width, and light shift of the CPT resonance spectrum analytically from the present multilevel atomic model. By calculating the model numerically with the experimentally determined decay rates of the ground and excited states, the amplitude and shape of the CPT resonance were obtained for different excitations by circular or linear polarization. We confirmed that the calculations accurately reproduced the experimental spectra observed in Cs-vapor cells and elucidated the mechanism underlying various characteristics. Specifically, we found that the Zeeman CPT spectra with different buffer gas pressures vary due to the relaxation process. Calculation using the present model confirmed that the observed pattern of the first-order Zeeman CPT spectra varies depending on the excitation scheme of polarization and the excitation level of $F' = 3$ or 4. The (m, m) CPT resonance [except for $(0, 0)$] appears in the second-order Zeeman CPT spectrum in the Lin || Lin excitation, which demonstrates the need for an additional condition to prohibit the CPT resonance. We also clarified that the amplitude for $\sigma^- - \sigma^-$ excitation saturates while that for Lin || Lin excitation increases in proportion to the excitation intensity coincident with a variation of the population of the trap state. The qualitative saturation in $\sigma^- - \sigma^-$ excitation can be reproduced by calculation with the four-level model. However, with the 32-level model, we can further reproduce the relative difference between the excited levels $F' = 3$ and 4, and the difference between other excitation schemes, such as the Lin \perp Lin polarization scheme. Thus, using the present 32-level model, we can know the features such as width,

amplitude, and symmetry of the CPT resonance under various specifications.

These findings indicate that our computational multilevel model can help clarify the phenomena of the CPT resonance and promote the development of miniature atomic clock devices. To further improve the multilevel atomic model, it would be necessary to add spatial characteristics of the Gaussian intensity distribution of the excitation light, the attenuation of light in the thickness direction, the saturation effect of one-photon absorption, the spatial nonuniformity of

the magnetic field, the interaction with extra sideband lights, and so on.

ACKNOWLEDGMENTS

This study was supported by Innovative Science and Technology Initiative for Security Grant No. JPJ004596, ATLA, Japan. K.M. thanks Dr. Yuichiro Yano of National Institute of Information and Communications Technology, for his kind introduction to his work.

APPENDIX: CPT SPECTRUM IN THE 32-LEVEL MODEL

Here we consider the shape of the CPT spectrum using the 32-level model. First, we introduce shorthand symbols to represent symmetric and asymmetric Lorentz functions, namely, $\mathcal{S}(x, w) = \frac{w}{x^2 + w^2}$ and $\mathcal{A}(x, w) = \frac{x}{x^2 + w^2} = \mathcal{S}(x, w) * x/w$. We can find $(w \pm ix)^{-1} = \mathcal{S}(x, w) \mp i\mathcal{A}(x, w)$. From the Liouville equation in Eq. (14), for indices $g = 1, \dots, 7$ and $i = 17, \dots, 32$, $\text{Im}(\Omega_{gi}\rho_{ig})$ is written as follows:

$$\text{Im}(\Omega_{gi}\rho_{ig}) = \frac{\mathcal{S}(\delta_i - \delta_g, \gamma_f)}{2} \left[|\Omega_{gi}|^2(\rho_{gg} - \rho_{ii}) + \text{Re} \left(\sum_{v=8}^{16} \Omega_{vi}\Omega_{ig}\rho_{gv} \right) - \frac{\delta_i - \delta_g}{\gamma_f} \text{Im} \left(\sum_{v=8}^{16} \Omega_{vi}\Omega_{ig}\rho_{gv} \right) \right]. \quad (\text{A1})$$

For simplicity, we ignore the coherence between any two magnetic sublevels in the same hyperfine state. In a similar manner, for indices $e = 8, \dots, 16$ and $i = 17, \dots, 32$, $\text{Im}(\Omega_{ei}\rho_{ie})$ is written as follows:

$$\text{Im}(\Omega_{ei}\rho_{ie}) = \frac{\mathcal{S}(\delta_i - \delta_e, \gamma_f)}{2} \left[|\Omega_{ei}|^2(\rho_{ee} - \rho_{ii}) + \text{Re} \left(\sum_{v=1}^7 \Omega_{ei}\Omega_{iv}\rho_{ve} \right) - \frac{\delta_i - \delta_e}{\gamma_f} \text{Im} \left(\sum_{v=1}^7 \Omega_{ei}\Omega_{iv}\rho_{ve} \right) \right]. \quad (\text{A2})$$

Here, we define transmittance T as $T = 1 - \alpha \sum_{n=17}^{32} \sum_{l=1}^{16} \rho_{ln} \text{Im}(\Omega_{ln}\rho_{nl})$, where $\alpha = \frac{N_{\text{atom}}\hbar\omega\Gamma}{(I_1 + I_2)S_{\text{beam}}}$. N_{atom} , $\hbar\omega$, and S_{beam} are the number of interacting atoms, the energy of a photon of the excitation light, and the cross section of the beam, respectively. Thus, T can be written as

$$T = 1 - \sum_{i'=17}^{32} \sum_{l'=1}^{16} \mathcal{F}_1(l', i') + \sum_{g'=1}^7 \sum_{e'=8}^{16} \mathcal{F}_2(g', e'), \quad (\text{A3})$$

$$\mathcal{F}_1(l, i) = \frac{\alpha}{2\Gamma} \mathcal{S}(\delta_i, \gamma_f) |\Omega_{li}|^2 (\rho_{ll} - \rho_{ii}), \quad \mathcal{F}_2(g, e) = -\frac{\alpha}{2\Gamma} \sum_{i=17}^{32} \mathcal{S}(\delta_i, \gamma_f) \text{Re}[\Omega_{ei}\Omega_{ig}\rho_{ge}], \quad (\text{A4})$$

where $\mathcal{S}(\delta_i - \delta_g, \gamma_f) \cong \mathcal{S}(\delta_i - \delta_e, \gamma_f)$ is replaced with $\mathcal{S}(\delta_i, \gamma_f)$. We also assume $|\delta_g - \delta_e| \ll \gamma_f$, as this is satisfied in typical situations for CPT resonance measurements. $\mathcal{F}_1(l, i)$ represents the one-photon absorption from $|l\rangle$ to $|i\rangle$. $\mathcal{F}_2(g, e)$ represents the CPT spectrum corresponding to the resonance state of $|g\rangle$ and $|e\rangle$. We now focus on the details of the CPT spectrum, $\mathcal{F}_2(g, e)$. From Eq. (18),

$$-\text{Re}(\Omega_{ig}\Omega_{ei}\rho_{ge}) = \mathcal{S}(\Delta_{ge-LS}, \Delta_{ge-w}) \text{Re}(\mathcal{M}) + \mathcal{A}(\Delta_{ge-LS}, \Delta_{ge-w}) \text{Im}(\mathcal{M}), \quad (\text{A5})$$

$$\mathcal{M} \cong \frac{1}{4} \sum_{u=17}^{32} \mathcal{S}(\delta_u - \gamma_f) \Omega_{ig}\Omega_{ei}\Omega_{gu}\Omega_{ue} \left[\left(1 - i \frac{\delta_u - \delta_e}{\gamma_f} \right) \rho_{ee} + \left(1 + i \frac{\delta_u - \delta_g}{\gamma_f} \right) \rho_{gg} \right]. \quad (\text{A6})$$

Here, we denote $\Delta_{ge-LS} = \delta_g - \delta_e - \Delta_{LS}$ and $\Delta_{ge-w} = \Delta_{\text{width}}$. In cases of $\sigma - \sigma$, $\text{Lin} \parallel \text{Lin}$, or $\text{Lin} \perp \text{Lin}$ excitations, one of the real or imaginary parts of $\Omega_{ig}\Omega_{ei}$ is zero for any values of $g = 1, \dots, 7$, $e = 8, \dots, 16$, and $i = 17, \dots, 32$, which can be confirmed from Eq. (8). Thus, $\Omega_{ig}\Omega_{ei}\Omega_{gu}\Omega_{ue}$ is a real value.

Since the Zeeman shift is negligibly small relative to the hyperfine splitting between $6P_{1/2}F' = 3$ and 4 levels (Δ'_{hfs} in Fig. 1), we can rewrite $\mathcal{S}(\delta_u, \gamma_f) = \mathcal{S}(\delta_{F'=3} = \Delta_{\text{opt}} + \frac{\Delta'_{\text{hfs}}}{2}, \gamma_f)$ for $u = 17, \dots, 23$ and $\mathcal{S}(\delta_u, \gamma_f) = \mathcal{S}(\delta_{F'=4} = \Delta_{\text{opt}} - \frac{\Delta'_{\text{hfs}}}{2}, \gamma_f)$ for $u = 24, \dots, 32$. When the excitation lights are tuned closely to either of the $F' = 3$ or 4 levels and $\Delta'_{\text{hfs}} \gg \gamma_f^2$ is satisfied, we can assume $\mathcal{S}(\delta_{F'=4}, \gamma_f) \ll \mathcal{S}(\delta_{F'=3}, \gamma_f)$ or $\mathcal{S}(\delta_{F'=3}, \gamma_f) \ll \mathcal{S}(\delta_{F'=4}, \gamma_f)$, respectively. Finally, we obtain the CPT spectrum in

the case of excitation to $F' = 3$ and 4 levels [$\mathcal{F}_2^{F'=3}(g, e)$ and $\mathcal{F}_2^{F'=4}(g, e)$, respectively] as follows:

$$\begin{aligned} & \mathcal{F}_2^{F'=3}(g, e) \\ &= \frac{\alpha}{8\Gamma} \mathcal{S}(\delta_{F'=3}, \gamma_f)^2 \left| \sum_{i=17}^{23} \Omega_{ig} \Omega_{ei} \right|^2 \left[\mathcal{S}(\Delta_{ge-LS}, \Delta_{ge-w})(\rho_{gg} + \rho_{ee}) + \mathcal{A}(\Delta_{ge-LS}, \Delta_{ge-w}) \frac{\delta_{F'=3}(\rho_{gg} - \rho_{ee}) - \delta_g \rho_{gg} + \delta_e \rho_{ee}}{\gamma_f} \right], \end{aligned} \quad (\text{A7})$$

$$\begin{aligned} & \mathcal{F}_2^{F'=4}(g, e) \\ &= \frac{\alpha}{8\Gamma} \mathcal{S}(\delta_{F'=4}, \gamma_f)^2 \left| \sum_{i=24}^{32} \Omega_{ig} \Omega_{ei} \right|^2 \left[\mathcal{S}(\Delta_{ge-LS}, \Delta_{ge-w})(\rho_{gg} + \rho_{ee}) + \mathcal{A}(\Delta_{ge-LS}, \Delta_{ge-w}) \frac{\delta_{F'=4}(\rho_{gg} - \rho_{ee}) - \delta_g \rho_{gg} + \delta_e \rho_{ee}}{\gamma_f} \right]. \end{aligned} \quad (\text{A8})$$

These are written as the sum of one symmetric and one asymmetric Lorentz function, whose width is Δ_{ge-w} and whose center is Δ_{ge-LS} .

-
- [1] G. Alzetta, A. Gozzini, M. Moi, and G. Orriols, *Nuovo Cimento B* **36**, 5 (1976).
- [2] E. Arimondo, *Prog. Opt.* **35**, 257 (1996).
- [3] J. Vanier, *Appl. Phys. B* **81**, 421 (2005).
- [4] N. Cyr, M. Têtu, and M. Breton, *IEEE Trans. Instrum. Meas.* **42**, 640 (1993).
- [5] F. Levi, A. Godone, C. Novero, and J. Vanier, On the use of a modulated laser for hyperfine frequency excitation in passive atomic frequency standards, in *Proceedings of 11th European Frequency and Time Forum* (Swiss Foundation for Research in Microtechnology, Switzerland, 1997), pp. 216–220.
- [6] J. Kitching, S. Knappe, and L. Hollberg, *Appl. Phys. Lett.* **81**, 553 (2002).
- [7] L.-A. Liew, S. Knappe, J. Moreland, H. Robinson, L. Hollberg, and J. Kitching, *Appl. Phys. Lett.* **84**, 2694 (2004).
- [8] S. Knappe, V. Shah, P. D. D. Schwindt, L. Hollberg, and J. Kitching, *Appl. Phys. Lett.* **85**, 1460 (2004).
- [9] J. Kiching, *Appl. Phys. Rev.* **5**, 031302 (2018).
- [10] P. Yun, R. Boudot, and E. de Clercq, *Phys. Rev. Appl.* **19**, 024012 (2023).
- [11] M. Abdel Hafiz, G. Coget, M. Petersen, C. Rocher, S. Guérandel, T. Zanon-Willette, E. de Clercq, and R. Boudot, *Phys. Rev. Appl.* **9**, 064002 (2018).
- [12] S. Yanagimachi, K. Harasaka, R. Suzuki, M. Suzuki, and S. Goka, *Appl. Phys. Lett.* **116**, 104102 (2020).
- [13] Y.-Y. Jau, E. Miron, A. B. Post, N. N. Kuzma, and W. Happer, *Phys. Rev. Lett.* **93**, 160802 (2004).
- [14] S. V. Kargapol'tsev, J. Kitching, L. Hollberg, A. V. Taichenachev, V. L. Velichansky, and V. I. Yudin, *Laser Phys. Lett.* **1**, 495 (2004).
- [15] T. Zanon, S. Guérandel, E. de Clercq, D. Holleville, N. Dimarcq, and A. Clairon, *Phys. Rev. Lett.* **94**, 193002 (2005).
- [16] A. V. Taichenachev, V. I. Yudin, V. L. Velichansky, and S. A. Zibrov, *JETP Lett.* **82**, 398 (2005).
- [17] X. Liu, J.-M. Mérola, S. Guérandel, C. Gorecki, E. de Clercq, and R. Boudot, *Phys. Rev. A* **87**, 013416 (2013).
- [18] E. A. Korsunsky and D. V. Kosachiov, *Phys. Rev. A* **60**, 4996 (1999).
- [19] G. Breit and I. I. Rabi, *Phys. Rev.* **38**, 2082 (1931).
- [20] K. Matsumoto, S. Kagami, A. Kirihara, S. Yanagimachi, T. Ikegami, and A. Morinaga, *Phys. Rev. A* **105**, 023110 (2022).
- [21] F. Levi, A. Godone, J. Vanier, S. Micalizio, and G. Modugno, *Eur. Phys. J. D* **12**, 53 (2000).
- [22] A. V. Taichenachev, V. I. Yudin, R. Wynands, M. Stähler, J. Kitching, and L. Hollberg, *Phys. Rev. A* **67**, 033810 (2003).
- [23] F. Renzoni, W. Maichen, L. Windholz, and E. Arimondo, *Phys. Rev. A* **55**, 3710 (1997).
- [24] Z. Warren, M. S. Shahriar, R. Tripathi, and G. S. Pati, *Metrologia* **54**, 418 (2017).
- [25] K. Matsuda, S. Goka, M. Kajita, and Y. Yano, Study of quantitative calculation of CPT resonances considering Zeeman sub-levels of Cs-D1 line, in *Proceedings of 2018 IEEE International Frequency Control Symposium* (IEEE, USA, 2018), pp. 403–405.
- [26] M. S. Shahriar, Y. Wang, S. Krishnamurthy, Y. Tu, G. S. Pati, and S. Tseng, *J. Mod. Opt.* **61**, 351 (2014).
- [27] D. A. Steck, Cesium D line data, available online at <http://steck.us/alkalidata> (revision 2.2.1, 21 November 2019).
- [28] M. Kajita, M. Tachikawa, and T. Shimizu, *J. Chem. Phys.* **87**, 1620 (1987).
- [29] S. Micalizio, A. Godone, F. Levi, and C. Calosso, *Phys. Rev. A* **79**, 013403 (2009).
- [30] J. Vanier and C. Audoin, *The Quantum Physics of Atomic Frequency Standards* (Hilger, London, 1989).
- [31] S. Knappe, M. Stähler, C. Affolderbach, A. V. Taichenachev, V. I. Yudin, and R. Wynands, *Appl. Phys. B* **76**, 57 (2003).
- [32] J. Ghosh, R. Ghosh, F. Goldfarb, J.-L. Le Gouët, and F. Bretenaker, *Phys. Rev. A* **80**, 023817 (2009).
- [33] L.-C. Ha, X. Zhang, N. Dao, and K. R. Overstreet, *Phys. Rev. A* **103**, 022826 (2021).
- [34] S. Micalizio and A. Godone, *Phys. Rev. A* **99**, 043425 (2019).